Contents lists available at ScienceDirect

Transactions of Nonferrous Metals Society of China

36(2026) 842−854

www.tnmsc.cn

Microstructural evolution and tensile deformation behaviors of fine-grained $Fe_{40}Mn_{20}Co_{20}Cr_{15}Si_5$ high entropy alloy prepared by friction stir processing

Jia LIN [a,#], Yuan FANG [b,#], Wen WANG [a,*], Peng HAN [a], Ting ZHANG [a], Qiang LIU [a], Ya-ting XIANG [a], Feng-ming QIANG [a], Ke QIAO [a,**], Kuai-she WANG [a]

[a] National and Local Joint Engineering Research Center for Functional Materials Processing, School of Metallurgical Engineering, Xi'an University of Architecture and Technology, Xi'an 710055, China;

[b] Xinjiang Xiangrun New Materials Technology Co., Ltd., Hami 839000, China

Abstract: A fine-grained metastable dual-phase $Fe_{40}Mn_{20}Co_{20}Cr_{15}Si_5$ high entropy alloy (CS-HEA) with excellent strength and ductility was successfully prepared by friction stir processing (FSP). The microstructural and mechanical properties of the fine-grained CS-HEA were characterized. The results showed that as-cast shrinkage cavities and elemental segregation were eliminated. The average grain size was refined from 121.1 to 5.4 μm. The face-centered cubic phase fraction increased from 23% to 82%. During tensile deformation, dislocation slip dominated at strains ranging from 5% to 17%, followed by transformation induced plasticity (TRIP) from 17% to 26%, and twin induced plasticity (TWIP) from 26% to 37%. The yield strength, ultimate tensile strength, and elongation of the fine-grained CS-HEA were 503 MPa, 1120 MPa, and 37%, respectively. The strength−ductility synergy of fine-grained CS-HEA was attributed to the combined effects of TRIP, TWIP, dislocation strengthening, and fine-grained strengthening.

Keywords: friction stir processing; metastable high entropy alloy; fine-grained microstructure; deformation behaviors; transformation-induced plasticity

1 Introduction

High entropy alloys (HEAs) are gaining attention due to their excellent strength [1], ductility [2], and fracture toughness [3]. These properties make them highly suitable for applications in the aerospace, railway, and petrochemical industries [4,5]. The $Fe_{40}Mn_{20}Co_{20}Cr_{15}Si_5$ HEA (CS-HEA) has a metastable dual phase structure, comprising both face-centered cubic (FCC) and hexagonal close-packed (HCP) phases [6]. This unique structure endows the alloy with transformation-induced plasticity (TRIP) and twin-induced plasticity (TWIP) effects, which contribute to its exceptional strength, ductility and work-hardening ability [7,8]. Consequently, CS-HEA is considered a promising candidate for applications, where both strength and ductility are crucial [9,10].

CS-HEA is susceptible to casting defects like elemental segregation, grain coarsening, and shrinkage due to its multi-element composition [11]. These casting defects significantly reduce strength and ductility of the material [12]. Therefore, post-casting treatments are necessary to modify the microstructure of the as-cast alloy. Such treatments typically involve severe plastic deformation methods like rolling [12], high-pressure torsion [13], and equal-channel angular pressing [14]. However, these processes can produce a multitude of low-angle grain

[#]Jia LIN and Yuan FANG contributed equally to this work

Corresponding author: [*]Wen WANG, Tel: +86-13720527194, E-mail: wangwen2025@126.com;
[**]Ke QIAO, Tel: +86-18149058901, E-mail: qiaoke_2020@126.com

https://doi.org/10.1016/S1003-6326(25)67001-4

Received 29 June 2024; accepted 28 April 2025

1003-6326/© 2026 The Nonferrous Metals Society of China. Published by Elsevier Ltd & Science Press

This is an open access article under the CC BY-NC-ND license (http://creativecommons.org/licenses/by-nc-nd/4.0/)

boundaries (LAGBs) because of grain fragmentation [15]. The accumulation of LAGBs restricts dislocation movement, thereby reducing material ductility [16].

Friction stir processing (FSP) is an advanced solid-state plastic deformation technique that achieves microstructural refinement, homogenization, and densification [17]. This process leverages a unique thermo-mechanical coupling effect to promote dynamic recrystallization (DRX) [16]. DRX enhances material strength and ductility by producing fine grains and a high fraction of high-angle grain boundaries (HAGBs). For instance, NENE et al [6] observed that FSP refined the grain size of cast CS-HEA. After FSP, the yield strength (YS), ultimate tensile strength (UTS), and elongation (EL) improved to 710 MPa, 990 MPa, and 22%, respectively. These mechanical properties represent increase of 65%, 44%, and 29% respectively over those of the base metal (BM). Thus, FSP effectively enhances both the strength and ductility of CS-HEA.

Current research focuses on how FSP process parameters affect the microstructure and properties of CS-HEA [18,19]. During FSP, the heat input and shear force are determined by the process parameters. The stirring tool provides high heat input and shear force by increasing rotation and reducing processing speeds, thereby promoting grain fragmentation, recrystallization, and refinement. This grain refinement enhances both strength and ductility [15]. NENE et al [6] also ascribe the simultaneous improvement in strength and ductility of FSP-treated CS-HEA to the transformation of the FCC phase. Compared to BM, FSP-treated CS-HEA exhibits a finer grain and higher FCC phase fraction, which modifies the deformation mechanisms. Notably, similar results have been observed in TRIP and TWIP steels [20,21].

In fine-grained CS-HEA, the TRIP effect facilitates substantial FCC to HCP phase transformations, extending the work-hardening stage and thus increasing elongation (EL) [6]. SINHA et al [19] found that the TWIP effect induces a dynamic Hall−Petch effect and significant back stress, enhancing work-hardening ability and ultimate tensile strength (UTS). Additionally, FRANK et al [8] observed that non-basal slip in the HCP phase can sustain large strains and delay plastic instability. These mechanisms, i.e., TRIP, TWIP, and non-basal slip, together enhance strength and ductility. However, their activation time and durations vary, with some potentially remaining inactive [19]. Understanding the individual effects of each mechanism requires a detailed analysis of tensile deformation behavior. However, previous studies have only inferred deformation mechanisms from microstructural changes before and after tensile testing, the interactive effects of these mechanisms during tensile deformation remain unexplored. Understanding these deformation mechanisms could guide for overcoming the problem of material strength and ductility synergy.

In this study, the fine-grained CS-HEA with excellent strength and ductility was successfully prepared by FSP and characterized its microstructure and room-temperature tensile deformation behavior. The microstructural evolution of the fine-grained CS-HEA during tensile deformation was investigated through interrupted tensile testing and quasi-in situ electron backscatter diffraction (EBSD) analysis. Furthermore, the tensile deformation mechanisms and their interactions were elucidated.

2 Experimental

2.1 Materials

As-received cast $Fe_{40}Mn_{20}Co_{20}Cr_{15}Si_5$ HEA plates prepared by electric arc furnace melting were selected as base metal (BM), and the chemical composition is shown in Table 1. The dimensions of CS-HEA plate are 130 mm × 60 mm × 4 mm (length × width × thickness).

Table 1 Chemical composition of $Fe_{40}Mn_{20}Co_{20}Cr_{15}Si_5$ (at.%)

Fe	Mn	Co	Cr	Si
39.48	19.94	21.59	14.41	4.58

2.2 Experimental methods

During FSP, a commercial friction stir welding machine (FSW-LMAM16-2D) was utilized operating at 500 r/min, with a processing speed of 50 mm/min and an inclination of 2°. The stirring tool, made of a W−Re alloy, had a concave shoulder of 12 mm in diameter and a conical pin of 2.3 mm in length, which gradually increased in diameter from 4 to 5 mm. Figure 1 shows a schematic diagram of the FSP.

The microstructure specimens were cut from the vertical processing direction (TD) with

dimensions of 20 mm × 4 mm × 5 mm (length × width × thickness) (Fig. 1). The microstructure was analyzed using a scanning electron microscope (SEM) equipped with EDS and EBSD (Gemini SEM 300). The EBSD specimens were mechanically polished with sandpaper, followed by electro-polishing to eliminate residual stresses from the surface. This process was achieved by preparing an electrolytic polishing solution consisting of 10 vol.% perchloric acid and 90 vol.% ethanol and applying a working voltage of 20 kV. The experimental data from EBSD were analyzed using Channel 5 software.

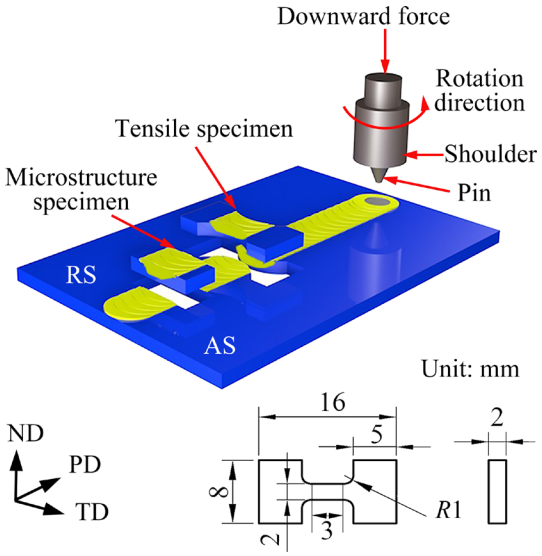

Fig. 1 Schematic diagram of FSP and dimension of tensile specimens: Normal direction (ND); Traverse direction (TD); Processing direction (PD); Advancing side (AS); Retreating side (RS)

The initial strain rate of $1.0\times10^{-3}\,s^{-1}$ was employed in the room temperature tensile test using an Instron 8801 testing machine. To ensure the accuracy of the data, three specimens were tested under identical parameters. The quasi-in situ EBSD analysis was applied to interrupting the tensile specimens. The interrupt tensile specimen dimensions, experimental equipment, and parameters were same as those used for the room temperature tensile test. During the interrupted tensile test, the specimen was subjected to 5% strain intervals. Strain levels of 0%, 5%, 10%, and 15% were applied during the tensile deformation. The dimensions and sampling position of the (interrupt) tensile specimen at room temperature are shown in Fig. 1.

2.3 Theoretical calculation of dislocation density

During tensile deformation, the material undergoes plastic deformation, resulting in the generation of a significant amount of geometrically necessary dislocations (GND) due to the lattice geometric constraints [20]. The GND density (ρ_{GND}) calculation formula is as follows [21]:

$$\rho_{GND} \approx \frac{\alpha\theta}{\mu b} \tag{1}$$

where α is a constant with a value of 3 [22], μ represents the scanning step distance in EBSD, b denotes the magnitude of Burgers vector (0.255 nm) [22], and θ represents the average value of kernel average misorientation (KAM). The calculation is as follows:

$$\theta = \exp\left[\frac{1}{N}\sum_{1}^{i}\ln \mathrm{KAM}_i\right] \tag{2}$$

where N refers to the number of points within the testing area, while KAM_i is the local value of KAM at point i.

3 Results and discussion

3.1 Microstructural characteristics of BM and FSP specimens

Figure 2 shows the microstructure of the BM. Shrinkage cavities can be observed in Fig. 2(a). The segregation of Fe, Mn, and Si can be observed in Fig. 2(b). The FCC and HCP phase fractions were 23% and 77%, respectively (Fig. 2(c)). The average grain size (GS) was 121.1 μm (Fig. 2(d)). The HCP phase was distributed in lamellar and blocky forms (Fig. 2(c)). Furthermore, the fractions of LAGBs (2°−15°) and HAGBs (>15°) were 25.3% and 74.7%, respectively (Fig. 2(e)).

After FSP, the shrinkage cavities and elemental segregation were eliminated (Figs. 3(a, b)), and the FCC and HCP phase fractions were 82% and 18%, respectively (Fig. 3(c)). Typically, high strain during processes like FSP induces a phase transformation from FCC to HCP. However, the FCC phase fraction was increased from 23% to 82% after FSP. Similarly, in a previous study, the FCC phase fraction increased when the rotational speed of the stirring tool exceeded a critical value at the same processing speed [6]. This phenomenon is attributed to the competition between thermal and mechanical effects. The phase transformation from HCP to FCC is

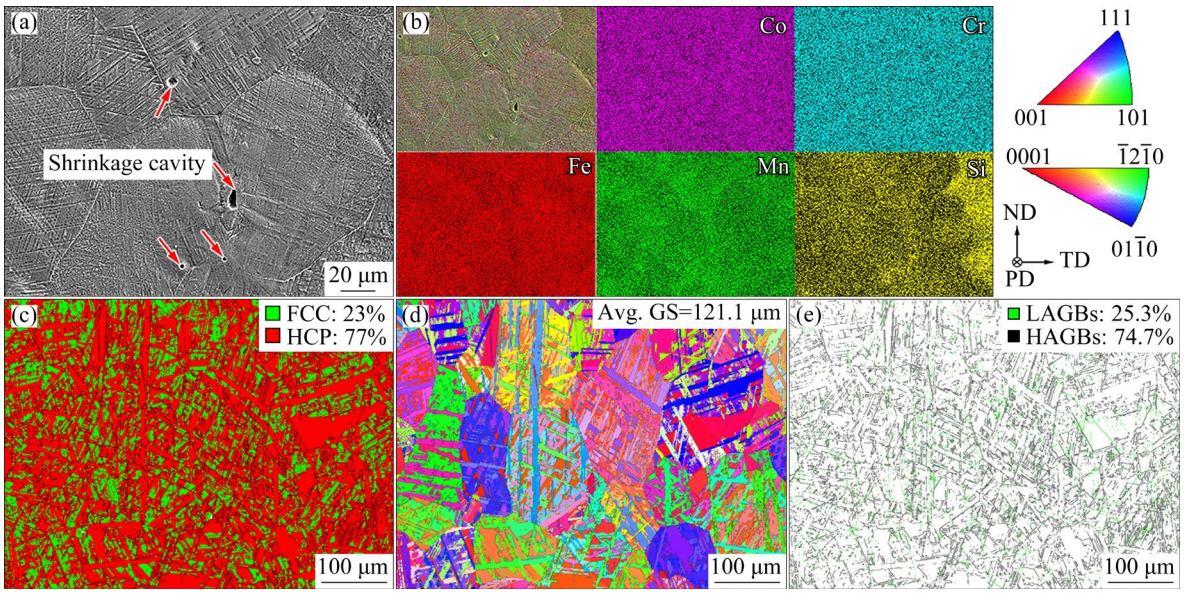

Fig. 2 Microstructure of BM specimen: (a) SEM morphology; (b) EDS elemental mapping images of area in (a); (c) Distribution of FCC and HCP phases; (d) Inverse pole figure (IPF) map and average grain size (GS); (e) Grain boundary map showing LAGBs and HAGBs

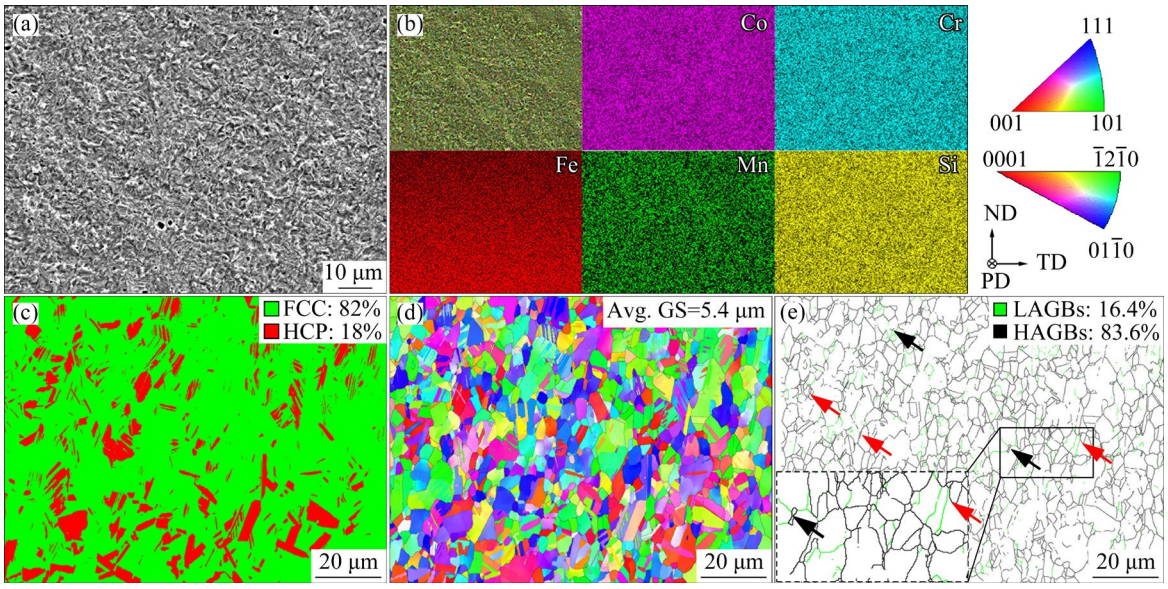

Fig. 3 Microstructure of FSP specimen: (a) SEM morphology; (b) EDS elemental mapping images of area in (a); (c) Distribution of FCC and HCP phases; (d) IPF map and average GS; (e) Grain boundary map showing LAGBs and HAGBs

promoted by thermal effects [23], whereas the reverse phase transformation from FCC to HCP is promoted by the mechanical effects [24]. Therefore, the increased FCC phase was promoted by the high thermal input.

FSP also refined the average grain size from 121.1 to 5.4 μm (Fig. 3(d)). Interrupted HAGBs appeared in regions where numerous LAGBs accumulated, which is typical of continuous dynamic recrystallization (CDRX, indicated by the black arrows in Fig. 3(e)). Additionally, some HAGBs exhibited a tongue-like morphology, which is typical of discontinuous dynamic recrystallization (DDRX, indicated by the red arrows in Fig. 3(e)). Grain refinement in the FSP CS-HEA was typically achieved through grain fragmentation, DDRX, and CDRX.

DDRX is commonly observed in materials

characterized by low stacking fault energy (SFE), while CDRX is predominantly observed in materials with high SFE [25]. However, in this study, CDRX occurred in the low-SFE CS-HEA. This was ascribed to the complex effects of temperature, strain, and dislocation movement [26]. In general, CDRX requires a low temperature and high strain rate [27]. The complex material flow during FSP generates localized regions characterized by low temperatures and high strain rates [28]. Additionally, dislocations in low-SFE CS-HEA tend to undergo planar slip or split into Shockley partial dislocations during deformation [29], which restricts cross-slip and leads to dislocation accumulation.

The LAGB fraction decreased from 25.3% to 16.4% after FSP (Fig. 3(e)). Often, severe plastic deformation techniques produce a large fraction of LAGBs. However, the LAGB fraction was lower after FSP. This is attributed to DRX, which promotes the aggregation of LAGBs and their transformation into HAGBs.

3.2 Tensile deformation behavior

3.2.1 Tensile properties

Figure 4(a) shows the engineering stress−strain curves of the BM and FSP specimens. The YS, UTS, and EL of the BM specimen were 257 MPa, 691 MPa, and 31%, respectively, whereas those of the FSP specimen were 503 MPa, 1120 MPa, and 37%, respectively, corresponding to increase of 96%, 62%, and 19%, respectively. This indicates that the strength and ductility of the material are simultaneously improved by FSP.

Figure 4(b) presents the work-hardening curves of the BM and FSP specimens. The FSP specimen exhibited a higher work-hardening ability than the BM specimen. The work-hardening curves were divided into three stages. In Stage I (5%−17% true strain for the FSP specimen), the work-hardening rate ($\partial\sigma/\partial\varepsilon$, where σ and ε are the true stress and strain, respectively) decreased rapidly. This decrease in work-hardening rate was attributed to dislocation slip in the initial stage of deformation, which reduced the work-hardening ability [30]. In Stage II (17%−26% true strain), the work-hardening rate stabilized. Finally, in Stage III (26%−37% true strain), the work-hardening rate decreased.

Figures 4(c, d) show the fracture morphologies of the BM and FSP specimens, respectively. The fracture surface of the BM specimen contained several cavities and tearing edges, demonstrating that the specimen failed by ductile-brittle mixed

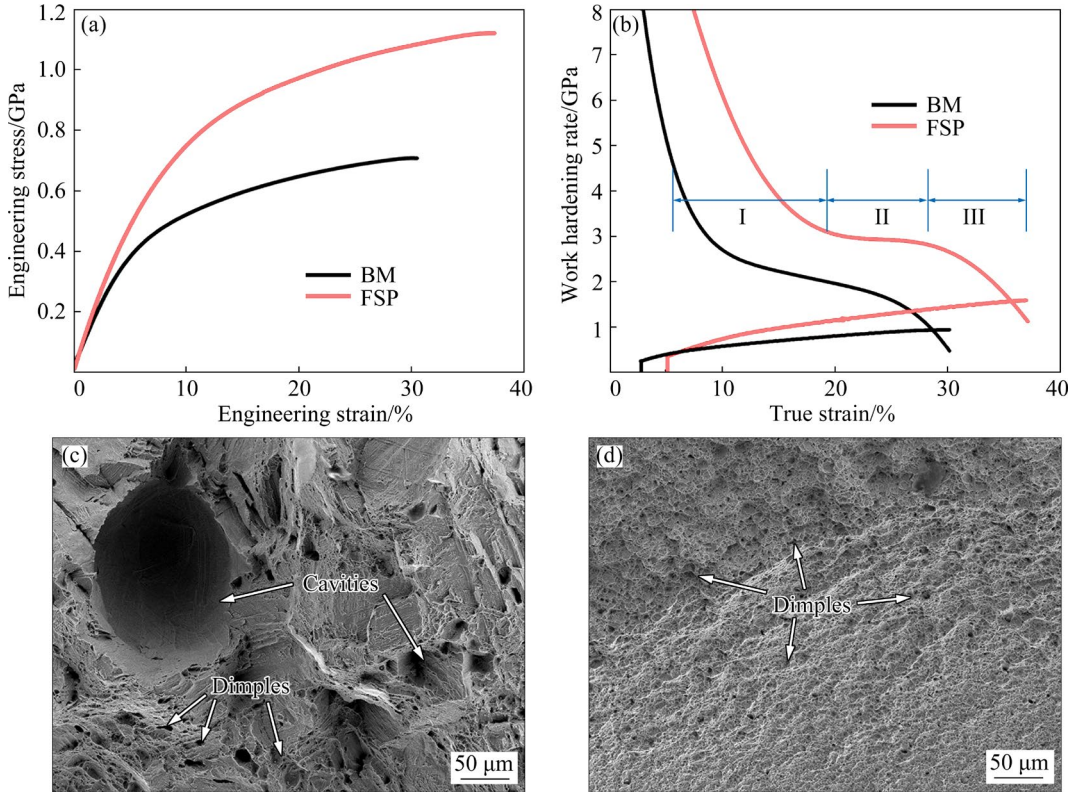

Fig. 4 Engineering stress−strain curves (a), strain hardening and true strain curves (b) of BM and FSP, and SEM images of fracture surfaces of BM (c) and FSP (d) specimens, respectively

fracture. For the FSP specimen, no cavities were observed, and fine dimples were distributed across the fracture surface, demonstrating that the specimen failed by ductile fracture. This indicates that the ductility of the as-cast CS-HEA is improved by FSP.

To quantitatively evaluate the work-hardening ability of the FSP specimen, the Hollomon equation ($\sigma=K\varepsilon^n$, where K is the strength coefficient, and n is the work-hardening index) [31] was used to fit the true stress−strain curve (Fig. 5). The fitting curves of the overall curve and Stages I−III were highly consistent with the experimental curve. The R^2 values of all fitting curves were above 0.99 (Table 2), demonstrating that the fitting results were reliable. The fitting parameters are listed in Table 2. The n value varies depending on the deformation mechanism [32]. The n values of Stages I, II, and III were 0.31, 0.41, and 0.40, respectively, indicating that n increased and then stabilized as the tensile loading increased. The n value in Stage II was 32% higher than that in Stage I, indicating that the work-hardening ability improved. In Stage III, the high n value (0.40) and long work-hardening stage delayed the necking of the specimen. Thus, the strength and ductility of the material were simultaneously enhanced by prolonging the work-hardening stage. According to Considère criterion, a high work-hardening rate delays necking and improves ductility [33−35]. At the same time, a high ductility enhances the storage capacity of dislocations and increases the strength.

3.2.2 Microstructural evolution of FSP specimen during tensile deformation

To explore the deformation mechanism of the FSP specimen during tensile testing, the microstructural evolution was characterized by quasi-in situ EBSD. Figures 6 shows the microstructure of the FSP specimen at engineering strains of 0%, 5%, 10%, and 15%, respectively. At a strain of 0%, the FCC and HCP phase fractions were 89% and 11%, respectively (Fig. 6(a_1)). Most of the HCP phase was distributed in a fine lamellar form, whereas some HCP phase was distributed in a block form (indicated by the white outline in Figs. 6(a_1) and (b_1)). This blocky HCP region comprised several fine lamellae. The fractions of the HAGBs and LAGBs were 52.2% and 47.8%, respectively (Fig. 6(c_1)).

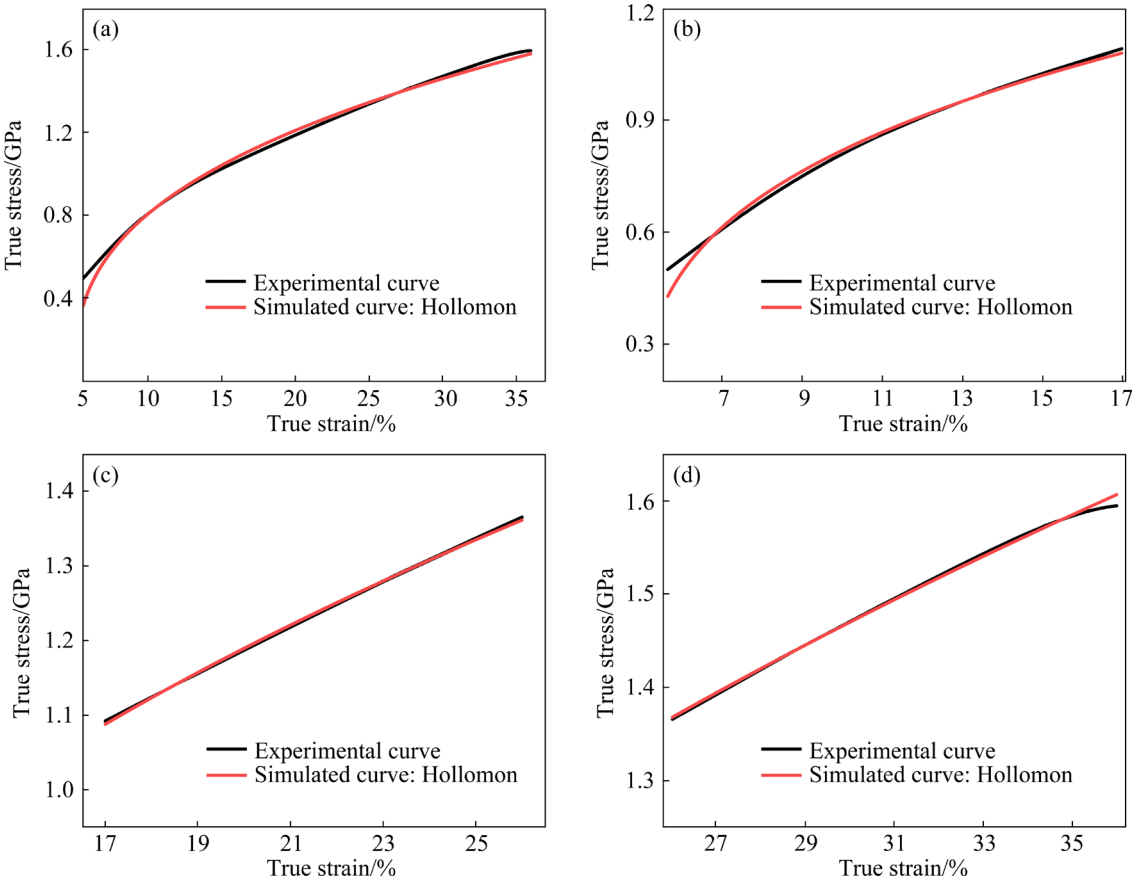

Fig. 5 Experimental true stress−strain curves of FSP specimen and fitted curves using Hollomon equation: (a) Overall curve; (b) Stage I: 5%−17%; (c) Stage II: 17%−26%; (d) Stage III: 26%−37%

Table 2 Simulated values of work-hardening index n, strengthening coefficient K, and coefficient of determination R^2 from Hollomon equation for FSP specimen

True strain/%	K/MPa	n	R^2
5−37 (overall curve)	2430	0.36	0.994
5−17 (Stage I)	2112	0.31	0.999
17−26 (Stage II)	2563	0.41	0.999
26−37 (Stage III)	2608	0.40	0.998

At a strain of 5%, the HCP phase fraction increased to 30% (Fig. 6(a_2)). Fine lamellar HCP phase nucleated within FCC grains, accompanied by blocky HCP regions consisting of several fine lamellae (Fig. 6(a_2)). The HCP phase formation was attributed to the generation of Shockley partial dislocations during deformation [28], leading to high-density dislocation accumulation that supplied the energy for the transformation to HCP. Notably, the HCP phase readily nucleated in coarse FCC grains but had difficulty in fine FCC grains (Figs. 6(a_2) and (b_2)). This was attributed to the high stability of the fine grains, which delayed the HCP phase transformation [28]. Figure 6(c_2) shows that there is a large fraction of LAGBs, indicating that dislocation slip occurred in this stage.

At a strain of 10%, the HCP phase fraction increased to 52% (Fig. 6(a_3)). Large amounts of HCP phase showed a block morphology. The orientation of these blocky regions was interrupted by the formation of twins (Fig. 6(b_3)). In addition, the LAGB fraction increased owing to intensive dislocation movement (Fig. 6(c_3)).

At a strain of 15%, the HCP phase fraction increased to 57% (Fig. 6(a_4)), indicating that the TRIP effect was weakened. The grains were elongated along the tensile direction, and numerous twins formed in the HCP phase (Fig. 6(b_4)). The LAGB fraction decreased slightly because the dislocation energy was consumed by twin formation (Fig. 6(c_4)). Based on the microstructural evolution, dislocation slip, TRIP-based phase transformation, and twinning occur sequentially during tensile deformation.

Figure 7 shows the HCP phase growth morphology and the orientation relationship between the FCC and HCP phases during tensile deformation. Two nucleation morphologies were observed. First, new HCP lamellae nucleated within FCC grains (solid circles in Figs. 7(a_2, b_2)). Second, fine laths of HCP nucleated at the FCC grain boundaries (dashed circles in Figs. 7(a_2, b_2)). These nucleation forms are similar to Types IV and II nucleation in the metastable dual-phase $Fe_{42}Co_{10}Cr_{15}Mn_{28}Si_5$ HEA [36]. Type IV nucleation is characterized by nucleation inside the FCC phase grains, with the

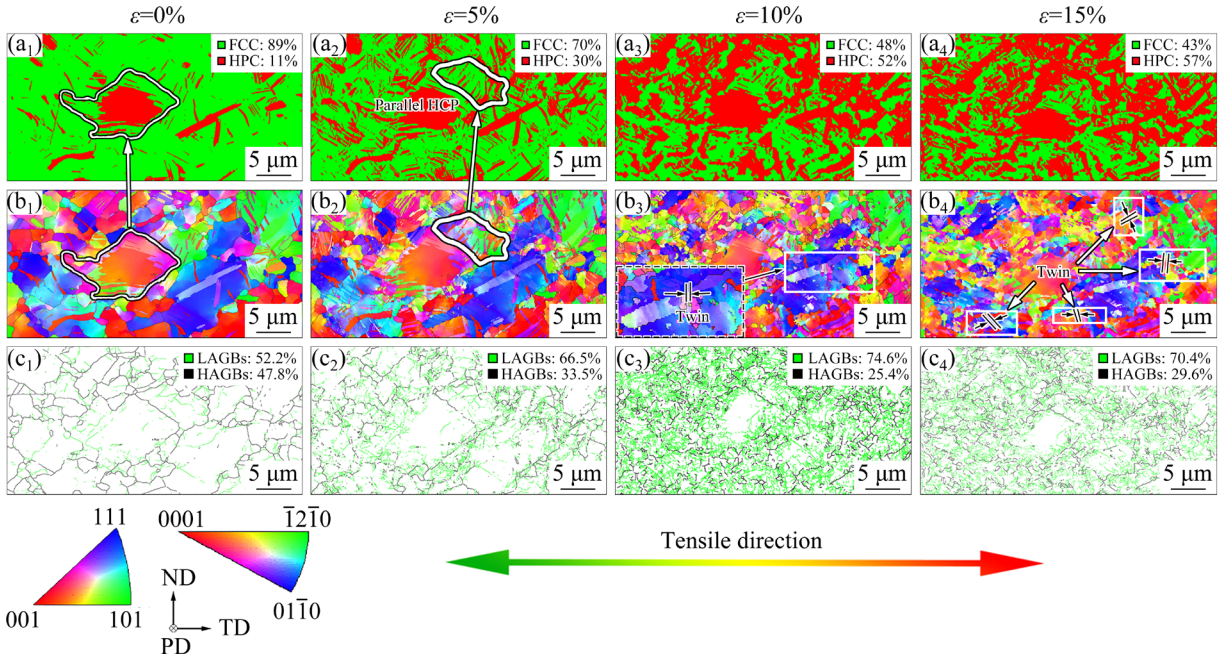

Fig. 6 Microstructural evolution of FSP specimen during quasi-in situ tensile test: (a_1−a_4) Phase distribution; (b_1−b_4) IPF; (c_1−c_4) Grain boundary map

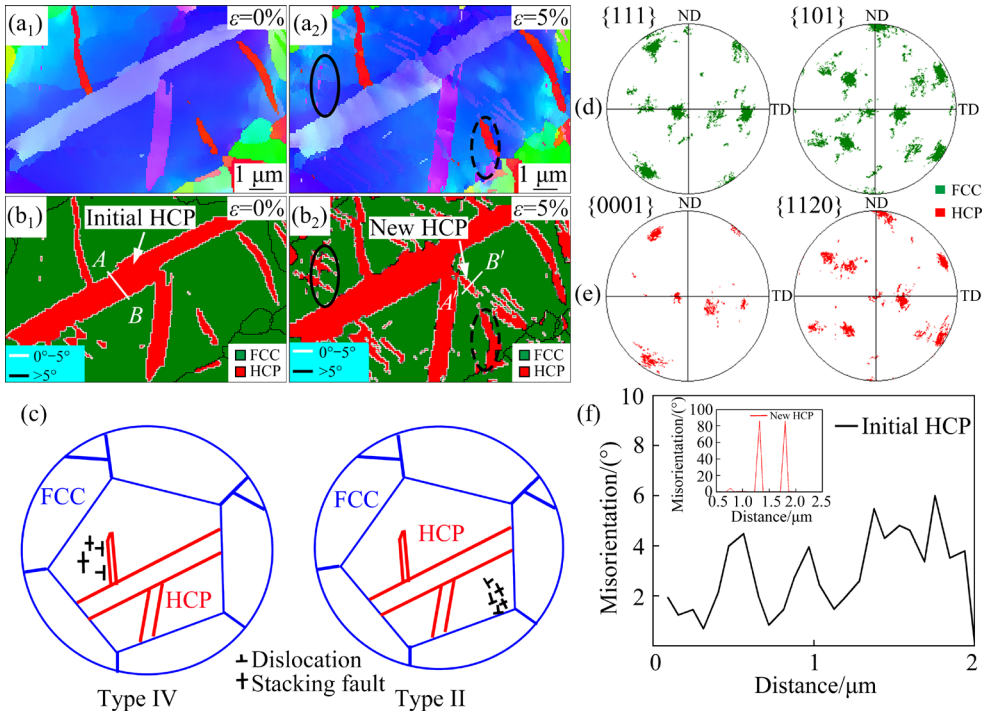

Fig. 7 HCP phase growth morphology and FCC/HCP orientation relationship (FSP specimen under tension): (a_1, a_2) IPF map; (b_1, b_2) Phase map; (c) Schematic of HCP growth; (d, e) Pole map of FCC/HCP phases (at 5% strain); (f) Misorientation of initial HCP along *A*−*B* (inset: new HCP along *A′*–*B′*)

nucleation sites provided by the interaction between stacking faults and dislocations (Fig. 7(c)). Type II nucleation is characterized by nucleation at the grain boundaries of the FCC phase, with the nucleation sites provided by the interaction between stacking faults and grain boundaries (Fig. 7(c)). In low-SFE CS-HEA, stacking faults easily interact with dislocations, resulting in Type IV nucleation [36]. However, Type II nucleation also occurs owing to grain refinement, which promotes the interaction between grain boundaries and stacking faults. Furthermore, the phase transformation from original FCC to HCP followed the S−N orientation relationship: $\{111\}_{FCC}//\{0001\}_{HCP}$, $\{10\bar{1}\}_{FCC}//\{11\bar{2}0\}_{HCP}$ (Figs. 7(d) and (e)).

Figure 7(f) depicts the misorientation degrees of both the initial and newly formed HCP phases. The initial HCP phase exhibited misorientation degrees of 1°−6°, suggesting the absence of twins [37]. In contrast, the newly formed HCP phase displayed a misorientation degree of 86° (inset of Fig. 7(f)), indicative of the formation of $\{11\bar{2}0\}$ tensile twins. The formation of these twins enhances both strength and ductility by hindering dislocation movement and reducing the average free path [21].

Figure 8 shows the KAM maps of the FCC and HCP phases at strains of 0%, 5%, and 10%, respectively. The KAM value is an indication of the severity of plastic deformation, with higher values reflecting severer deformation. With the strain increase from 0% to 5%, the KAM values increase along the phase boundary, indicating that dislocations accumulate along the phase boundary. At strain of 5%, Fig. 8(b_2) reveals that several fine HCP lamellae show high KAM values, coinciding with a substantial transformation of FCC to HCP phase as shown in Fig. 6(a_2). Thus, the primary deformation mechanisms at this stage were dislocation slip and TRIP-based phase transformation. At strain of 10%, KAM values increased for both FCC and HCP phases (Figs. 8(a_3) and (b_3)), with particularly high values in the HCP phase (Fig. 8(b_3)). In certain regions, twin formation disrupted the KAM distribution of the HCP phase (Fig. 8(b_3)). These observations suggest that the main deformation mechanisms at this stage are TRIP-based phase transformation and twinning. Data from the KAM map at 15% strain were deemed unreliable.

Figure 9(a) illustrates the variation in the FCC phase fraction and twin boundary fractions during tensile deformation. Between strains 10% and 15%,

the FCC phase fraction decreased at a slower rate, indicating that the TRIP effect weakened. Concurrently, the fractions of tensile and compressive twin boundaries increased rapidly, indicating a strengthened TWIP effect. Figure 9(b) shows the GND densities in the FCC and HCP phases at different strains. The GND densities of the FCC and HCP phases both increased between 0 and 5% strain but decreased between strains 5% and 10%. This phenomenon was attributed to dislocation energy consumed by TRIP and TWIP effects. Overall, these results demonstrate that dislocation slip, TRIP, and TWIP deformation mechanisms occurred successively with increasing strain. The strength and ductility were simultaneously improved by these deformation mechanisms.

3.2.3 Deformation mechanisms of FSP specimen

The enhancement in strength and ductility following FSP was attributed to the combined effects of dislocation slip, TRIP, and TWIP deformation mechanisms, which extended the work-hardening stage (Fig. 10). Table 3 lists the true stress increment ($\Delta\sigma$) and true strain increment ($\Delta\varepsilon$) for FSP and BM specimens over each hardening stage. At each stage, the $\Delta\sigma$ of the FSP specimen exceeded that of the BM specimen. During Stage I, $\Delta\sigma$ of the FSP specimen was 228 MPa higher than that of the BM specimen, indicating a significant enhancement in strength. As shown in Fig. 10, deformation mechanisms of the FSP specimen during this stage were dislocation slip and TRIP-based phase transformation. Dislocation entanglement and cells formation easily occur via planar slip in low-SFE CS-HEA [26]. Stacking faults easily interact with the dislocations and consume the dislocation energy [38,39]. Additionally, a minor portion of the HCP phase, with limited slip systems, underwent transformation via the TRIP effect (Fig. 6(a_2)). The movement of dislocations was therefore hindered by dislocation entanglement, dislocation cells, stacking faults, and HCP phases, resulting in enhanced strength [37,39]. Ultimately, the specimen displayed back-stress strengthening due to its heterogeneous microstructure of FCC and HCP phases [40].

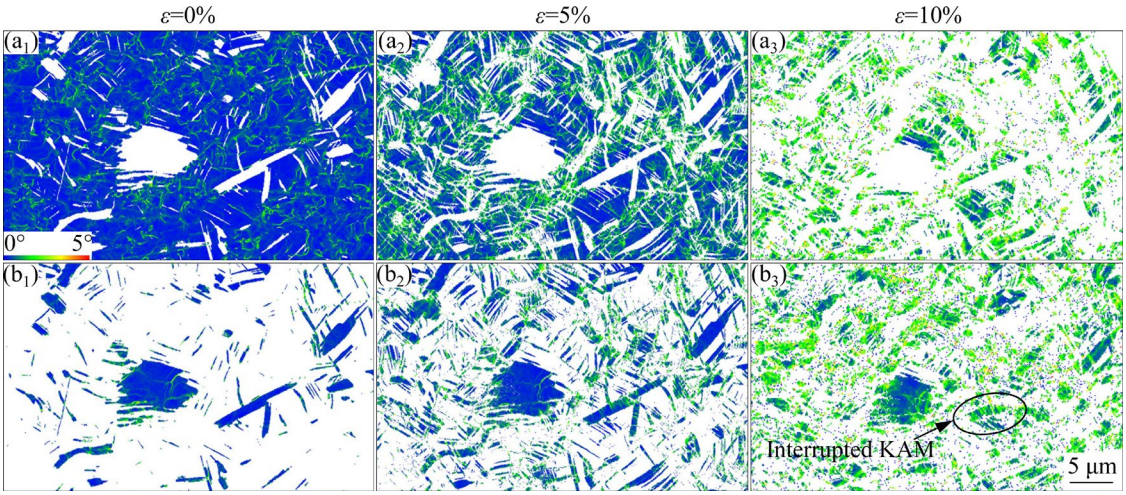

Fig. 8 KAM maps of FSP specimens: (a_1–a_3) FCC phase; (b_1–b_3) HCP phase

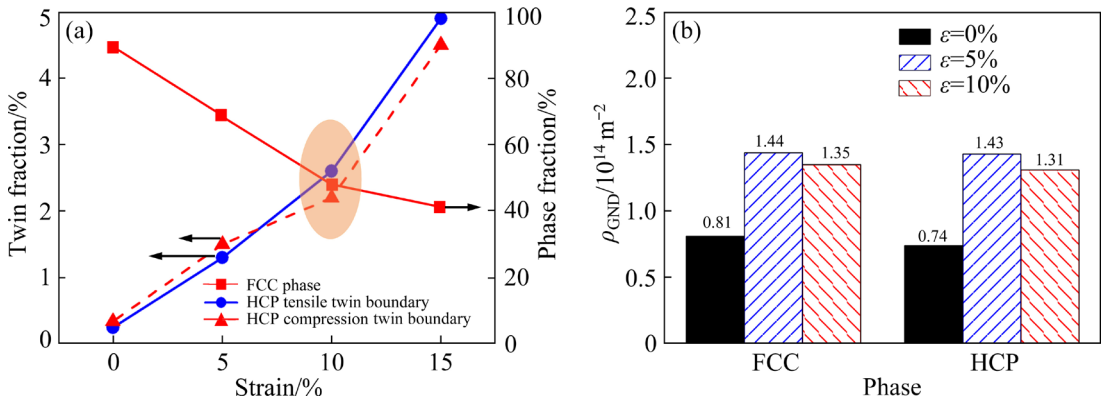

Fig. 9 Variation in fractions of twin boundaries and FCC phase (a), and GND density (b) during tensile testing

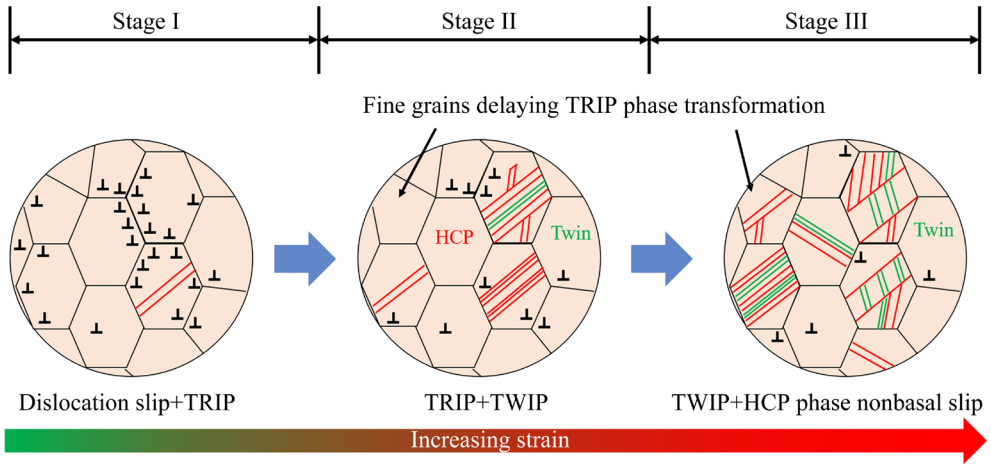

Fig. 10 Deformation mechanism and microstructural evolution with increasing strain

Table 3 Variation in true strain ($\Delta\sigma$) and true stress ($\Delta\varepsilon$) for BM and FSP specimens during work-hardening

Specimen	True strain/%	$\Delta\sigma$/MPa	$\Delta\varepsilon$/%
BM	2−10 (Stage I)	326	8
	10−24 (Stage II)	299	14
	24−31 (Stage III)	85	7
FSP	5−17 (Stage I)	554	12
	17−26 (Stage II)	394	9
	26−37 (Stage III)	141	11

The $\Delta\varepsilon$ of the FSP specimen was higher than that of the BM specimen during Stages I and III (Table 3), indicating an improvement in ductility. In Stage I, the main deformation mechanisms of the FSP specimen were dislocation slip and TRIP-based phase transformation. The dislocation slip was enhanced by the substantial FCC phase, which has multiple slip systems [8]. Furthermore, the TRIP-based transformation from FCC to HCP was a displacive process driven by atomic shearing, which can enhance the strain capacity of a workpiece [41,42]. In Stage III, the primary deformation mechanism was twinning (Fig. 10). The TWIP effect not only sustained the strain but also transformed the crystal orientation to one favorable dislocation slip [43,44]. The dynamic Hall−Petch effect, activated by the TWIP effect during tensile deformation, led to grain refinement and improved ductility. Additionally, non-basal slip was promoted by the increased HCP phase fraction, further improving the ductility [45].

The TRIP effect, activated in Stage II of the tensile deformation, also played a crucial role in extending the work-hardening stage. In the fine-grained CS-HEA, high critical stress for TRIP delayed its activation, extending the dislocation slip stage (Figs. 6(a_2) and (b_2)). After FSP, the specimen contained a large fraction of FCC phase, which extended the TRIP effect and promoted the activation of the TWIP effect. Strength and ductility improved together due to the grain refinement and increased FCC phase fraction. Figure 11 shows the relationship between the FCC phase fraction and strength ductility index SDI of the FSP CS-HEA specimen and other alloys [46]. The SDI quantifies the strength−ductility synergy during uniform tensile deformation. The SDI of the FSP CS-HEA in this study was higher than that of other advanced dual-phase HEAs (DP-HEAs) and other CS-HEAs prepared with different process parameters. Notably, the FSP CS-HEA, with a grain size of 5.4 μm and

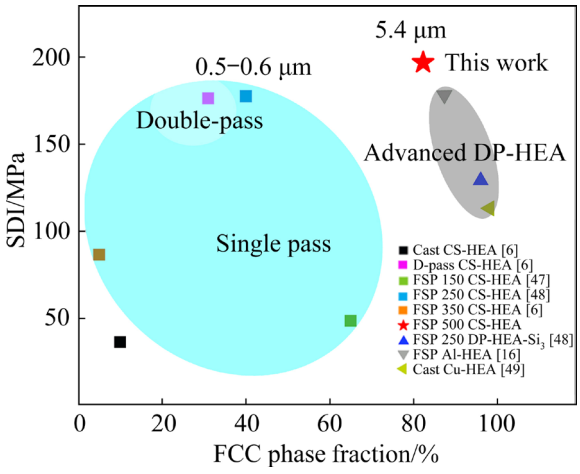

Fig. 11 Relationship between strength ductility index (SDI=(UTS−YS)×plastic strain) and face-centered cubic (FCC) phase fraction before tensile test

82% FCC phase, had a higher SDI than the nanocrystalline CS-HEA (0.5−0.6 μm), indicating that increasing the FCC phase fraction is more critical for strength−ductility synergy than refining grain size.

4 Conclusions

(1) After FSP, the shrinkage cavities of the as-cast CS-HEA were eliminated, and the elemental distribution was homogenized. CDRX and DDRX occurred during FSP, which refined the grain size from 121.1 to 5.4 μm. Furthermore, the FCC phase fraction increased from 23% to 82% due to the thermo-mechanical coupling effect.

(2) The strength and ductility of the FSP CS-HEA were simultaneously improved by grain refinement and phase transformation, which facilitated the TRIP and TWIP effects and extended the work-hardening stage. The YS, UTS, and EL of the FSP specimen were 503 MPa, 1120 MPa, and 37%, respectively, which were 96%, 62%, and 19% higher, respectively, than those of the BM.

(3) During tensile deformation, two HCP nucleation forms were observed: lamellar HCP nucleated inside the FCC grains, whereas fine laths of HCP nucleated at the FCC grain boundaries. The phase transformation from FCC to HCP followed the S−N orientation relationship: $\{111\}_{FCC}//\{0001\}_{HCP}$, $\{10\bar{1}\}_{FCC}//\{11\bar{2}0\}_{HCP}$.

CRediT authorship contribution statement

Jia LIN: Investigation, Characterization, Data interpretation, Visualization, Validation, Writing − Original draft, Writing − Review & editing; **Yuan FANG:** Data curation, Visualization, Validation; **Wen WANG:** Resources, Funding acquisition, Writing − Review & editing; **Peng HAN:** Conceptualization, Writing − Review & editing; **Ting ZHANG:** Supervision, Writing − Review & editing; **Qiang LIU:** Supervision, Writing − Review & editing; **Ya-ting XIANG:** Validation; **Feng-ming QIANG:** Supervision; **Ke QIAO:** Project administration; **Kuai-she WANG:** Funding acquisition.

Declaration of competing interest

The authors declare that they have no known competing financial interests or personal relationships that could have appeared to influence the work reported in this paper.

Acknowledgments

The authors gratefully acknowledge the funds of the National Natural Science Fund for Excellent Young Scholars of China (No. 52222410), Shaanxi Province National Science Fund for Distinguished Young Scholars, China (No. 2022JC-24), and the National Natural Science Foundation of China (Nos. 52227807, 52034005).

References

[1] YEH J W, CHEN S K, LIN S J, GAN J Y, CHIN T S, SHUN T T, TSAU C H, CHANG S Y. Nanostructured high-entropy alloys with multiple principal elements: Novel alloy design concepts and outcomes [J]. Advanced Engineering Materials, 2004, 6: 299−303.

[2] CANTOR B, CHANG I T H, KNIGHT P, VINCENT A J B. Microstructural development in equiatomic multicomponent alloys [J]. Materials Science and Engineering: A, 2004, 375/376/377: 213−218.

[3] GAO Xue-feng, CHEN Yao, REN Hao, QIN Gang, ZHOU Qi-wen, CHEN Rui-run, GUO Jing-jie. Tensile properties and strengthening behavior of CoCrFeNiW high entropy alloys with heterogeneous structures [J]. Transactions of Nonferrous Metals Society of China, 2024, 34(1): 890−904.

[4] GUO Lin, GU Ji, DAI Yi-long, LIN Jian-guo, SONG Min. Heterogeneous microstructure and mechanical properties of carbon-doped FeCoCrNiMn high-entropy alloy [J]. Transactions of Nonferrous Metals Society of China, 2024, 34(6): 1893−1907.

[5] ZHANG T W, MA S G, ZHAO D, WU Y C, ZHANG Y, WANG Z H, QIAO J W. Simultaneous enhancement of strength and ductility in a NiCoCrFe high-entropy alloy upon dynamic tension: Micromechanism and constitutive modeling [J]. International Journal of Plasticity, 2020, 124: 226−246.

[6] NENE S S, FRANK M, LIU K, SINHA S, MISHRA R S, MCWILLIAMS B A, CHO K C. Reversed strength-ductility relationship in microstructurally flexible high entropy alloy [J]. Scripta Materialia, 2018, 154: 163−167.

[7] MISHRA R S, NENE S S. Some unique aspects of mechanical behavior of metastable transformative high entropy alloys [J]. Metallurgical and Materials Transactions A, 2021, 52: 889−896.

[8] FRANK M, CHEN Y, NENE S S, SINHA S, LIU K, AN K, MISHRA R S. Investigating the deformation mechanisms of a highly metastable high entropy alloy using in-situ neutron diffraction [J]. Materials Today Communications, 2020, 23: 100858.

[9] GUPTA S, AGRAWAL P, NENE S S, MISHRA R S. Friction stir welding of γ-fcc dominated metastable high entropy alloy: Microstructural evolution and strength [J]. Scripta Materialia, 2021, 204: 114161.

[10] SALLOOM R, BASKES M I, SRINIVASAN S G. Atomic level simulations of the phase stability and stacking fault energy of FeCoCrMnSi high entropy alloy [J]. Modelling and Simulation in Materials Science and Engineering, 2022, 30: 075002.

[11] LI Z M, RAABE D. Strong and ductile non-equiatomic high-

entropy alloys: Design, processing, microstructure, and mechanical properties [J]. JOM, 2017, 69: 2099−2106.

[12] LI Z M, TASAN C C, PRADEEP K G, RAABE D. A TRIP-assisted dual-phase high-entropy alloy: Grain size and phase fraction effects on deformation behavior [J]. Acta Materialia, 2017, 131: 323−335.

[13] NGUYEN N T, ASGHARI-RAD P, SATHIYAMOORTHI P, ZARGARAN A, LEE C S, KIM H S. Ultrahigh high-strain-rate superplasticity in a nanostructured high-entropy alloy [J]. Nature Communications, 2020, 11: 2736.

[14] SHAHMIR H, MOUSAVI T, HE J Y, LU Z P, KAWASAKI M, LANGDON T G. Microstructure and properties of a CoCrFeNiMn high-entropy alloy processed by equal-channel angular pressing [J]. Materials Science and Engineering: A, 2017, 705: 411−419.

[15] BHOWMIK S, ZHANG J Z, VOGEL S C, NENE S S, MISHRA R S, MCWILLIAMS B A, KNEZEVIC M. Effects of plasticity-induced martensitic transformation and grain refinement on the evolution of microstructure and mechanical properties of a metastable high entropy alloy [J]. Journal of Alloys and Compounds, 2022, 891: 161871.

[16] KOMARASAMY M, KUMAR N, TANG Z, MISHRA R S, LIAW P K. Effect of microstructure on the deformation mechanism of friction stir-processed $Al_{0.1}CoCrFeNi$ high entropy alloy [J]. Materials Research Letters, 2015, 3: 30−34.

[17] HAN Peng, LIN Jia, WANG Wen, LIU Zhi-hao, XIANG Ya-ting, ZHANG Ting, LIU Qiang, GUAN Xiao-hu, QIAO Ke, XIE Ying-chun, WANG Kuai-she. Friction stir processing of cold-sprayed high-entropy alloy particles reinforced aluminum matrix composites: Corrosion and wear properties [J]. Metals and Materials International, 2023, 29 (3): 845−860.

[18] MISHRA R S, NENE S S, FRANK M, SINHA S, LIU K, SHUKLA S. Metastability driven hierarchical microstructural engineering: Overview of mechanical properties of metastable complex concentrated alloys [J]. Journal of Alloys and Compounds, 2020, 842: 155625.

[19] SINHA S, NENE S S, FRANK M, LIU K, LEBENSOHN R A, MISHRA R S. Deformation mechanisms and ductile fracture characteristics of a friction stir processed transformative high entropy alloy [J]. Acta Materialia, 2020, 184: 164−178.

[20] SNEHI M S, ANJABIN N, KIM H S. Study of geometrically necessary dislocations of a partially recrystallized aluminum alloy using 2D EBSD [J]. Microscopy and Microanalysis, 2019, 25: 656−663.

[21] QIAO Ke, WANG Kuai-she, WANG Jia, HAO Zheng-yang, XIANG Ya-ting, HAN Peng, CAI Jun, YANG Qi, WANG Wen. Microstructural evolution and deformation behavior of friction stir welded twin-induced plasticity steel [J]. Journal of Materials Science & Technology, 2024, 169: 68−81.

[22] YANG Fei, DONG Li-ming, CAI Lei, HU Xian-jun, FANG Feng. Mechanical properties of FeMnCoCr high entropy alloy alloyed with C/Si at low temperatures [J]. Journal of Alloys and Compounds, 2021, 859: 157876.

[23] SHEN Jia-jia, AGRAWAL P, RODRIGUES T A, LOPES J G, SCHELL N, HE Jing-jing, ZENG Zhi, MISHRA R S, OLIVEIRA J P. Microstructure evolution and mechanical properties in a gas tungsten arc welded $Fe_{42}Mn_{28}Co_{10}Cr_{15}Si_5$ metastable high entropy alloy [J]. Materials Science and Engineering: A, 2023, 867: 144722.

[24] SU Jing, WU Xiao-xiang, RAABE D, LI Zhi-ming. Deformation-driven bidirectional transformation promotes bulk nanostructure formation in a metastable interstitial high entropy alloy [J]. Acta Materialia, 2019, 167: 23−39.

[25] HEIDARZADEH A, SAEID T, KLEMM V, CHABOK A, PEI Y T. Effect of stacking fault energy on the restoration mechanisms and mechanical properties of friction stir welded copper alloys [J]. Materials & Design, 2019, 162: 185−197.

[26] LIU Ren-guang, TANG Jing, JIANG Jia-xi, LI Xiao-yan, WEI Yu-jie. Stacking fault induced hardening and grain size effect in nanocrystalline CoNiCrFeMn high-entropy alloy [J]. Extreme Mechanics Letters, 2022, 56: 101875.

[27] HEIDARZADEH A, MIRONOV S, KAIBYSHEV R, ÇAM G, SIMAR A, GERLICH A, KHODABAKHSHI F, MOSTAFAEI A, FIELD D P, ROBSON J D, DESCHAMPS A, WITHERS P J. Friction stir welding/processing of metals and alloys: A comprehensive review on microstructural evolution [J]. Progress in Materials Science, 2021, 117: 100752.

[28] LIN P T, LIU H C, HSIEH P Y, WEI C Y, TSAI C W, SATO Y S, CHEN S C, YEN H W, LU N H, CHEN C H. Heterogeneous structure-induced strength-ductility synergy by partial recrystallization during friction stir welding of a high-entropy alloy [J]. Materials & Design, 2021, 197: 109238.

[29] KUMAR S S, MURUGAN N, RAMACHANDRAN K K. Microstructure and mechanical properties of friction stir welded AISI 316L austenitic stainless steel joints [J]. Journal of Materials Processing Technology, 2018, 254: 79−90.

[30] NENE S S, FRANK M, LIU K, MISHRA R S, MCWILLIAMS B A, CHO K C. Extremely high strength and work hardening ability in a metastable high entropy alloy [J]. Scientific Reports, 2018, 8: 9920.

[31] JIANG Wei, GAO Xu-zhou, GUO Ya-zhou, CHEN Xiang, ZHAO Yong-hao. Dynamic impact behavior and deformation mechanisms of $Cr_{26}Mn_{20}Fe_{20}Co_{20}Ni_{14}$ high-entropy alloy [J]. Materials Science and Engineering: A, 2021, 824: 141858.

[32] WEI Q, CHENG S, RAMESH K T, MA E. Effect of nanocrystalline and ultrafine grain sizes on the strain rate sensitivity and activation volume: fcc versus bcc metals [J]. Materials Science and Engineering: A, 2004, 381: 71−79.

[33] MEI Jia-he, HAN Ying, ZU Guo-qing, ZHU Wei-wei, ZHAO Yu, CHEN Hua, RAN Xu. Achieving superior strength and ductility of AlSi10Mg alloy fabricated by selective laser melting with large laser power and high scanning speed [J]. Acta Metallurgica Sinica (English Letters), 2022, 35(10): 1665−1672.

[34] AHMED M Z, CHADHA K, REDDY S R, SHAHRIARI D, BHATTACHARJEE P P, JAHAZI M. Influence of process parameters on microstructure evolution during hot deformation of a eutectic high-entropy alloy (EHEA) [J]. Metallurgical and Materials Transactions A, 2020, 51: 6406−6420.

[35] ZHANG Zhen-jun, QU Zhan, XU Ling, LIU Rui, ZHANG Peng, ZHANG Zhe-feng. LANGDON T G. Relationship between strength and uniform elongation of metals based on an exponential hardening law [J]. Acta Materialia, 2022, 231: 117866.

[36] SITTIHO A, BHATTACHARYYA M, GRAVES J, NENE S S, MISHRA R S, CHARIT I. Friction stir processing of a high entropy alloy $Fe_{42}Co_{10}Cr_{15}Mn_{28}Si_5$ with transformative characteristics: Microstructure and mechanical properties [J]. Materials Today Communications, 2021, 28: 102635.
[37] NENE S S, AGRAWAL P, FRANK M, WATTS A, SHUKLA S, MORPHEW C, CHESETTI A, PARK J S, MISHRA R S. Transformative high entropy alloy conquers the strength-ductility paradigm by massive interface strengthening [J]. Scripta Materialia, 2021, 203: 114070.
[38] XIAO Jian-wei, WU Nan, OJO O, DENG Chuang. Stacking fault and transformation-induced plasticity in nanocrystalline high-entropy alloys [J]. Journal of Materials Research, 2021, 36: 2705−2714.
[39] SU Rui-zhe, NEFFATI D, ZHANG Yi-fan, CHO J, LI Jin, WANG Hai-yan, KULKARNI Y, ZHANG Xing-hang. The influence of stacking faults on mechanical behavior of advanced materials [J]. Materials Science and Engineering: A, 2021, 803: 140696.
[40] YANG Guang-hui, KIM J K. Hierarchical precipitates, sequential deformation-induced phase transformation, and enhanced back stress strengthening of the micro-alloyed high entropy alloy [J]. Acta Materialia, 2022, 233: 117974.
[41] YOU Z Y, TANG Z Y, CHU F B, MA L, GUAN G F, DING H, MISRA R D K. Microstructural design and deformation behavior of a TRIP/TWIP tri-phase heterogeneous high-entropy alloy [J]. Intermetallics, 2023, 156: 107854.
[42] SOHRABI M J, MIRZADEH H, SADEGHPOUR S, MAHMUDI R. Grain size dependent mechanical behavior and TRIP effect in a metastable austenitic stainless steel [J]. International Journal of Plasticity, 2023, 160: 103502.
[43] KALSAR R, SANAMAR S, SCHELL N, BROKMEIER H G, SAHA R, GHOSH P, SUWAS S. In-situ study of tensile deformation behaviour of medium Mn TWIP/TRIP steel using synchrotron radiation [J]. Materials Science and Engineering: A, 2022, 857: 144013.
[44] LAVAKUMAR A, YOSHIDA S, PUNYAFU J, IHARA S, CHONG Y, SAITO H, TSUJI N, MURAYAMA M. Yield and flow properties of ultra-fine, fine, and coarse grain microstructures of FeCoNi equiatomic alloy at ambient and cryogenic temperatures [J]. Scripta Materialia, 2023, 230: 115392.
[45] WANG Wen, HAN Peng, PENG Pai, GUO Hong-ju, HUANG Li-ying, QIAO Ke, HAI Min-na, YANG Qi, WANG Hong-duo, WANG Kuai-she, WANG Li-qiang. Superplastic deformation behavior of fine-grained AZ80 magnesium alloy prepared by friction stir processing [J]. Journal of Materials Research and Technology, 2020, 9(3): 5252−5263.
[46] NENE S S, SINHA S, FRANK M, LIU K, MISHRA R S, MCWILLIAMS B A, CHO K C. Unexpected strength−ductility response in an annealed, metastable, high-entropy alloy [J]. Applied Materials Today, 2018, 13: 198−206.
[47] AGRAWAL P, GUPTA S, SHUKLA S, NENE S S, THAPLIYAL S, TOLL M P, MISHRA R S. Role of Cu addition in enhancing strength-ductility synergy in transforming high entropy alloy [J]. Materials & Design, 2022, 215: 110487.
[48] LIU K, NENE S S, FRANK M, MISHRA R S. Effect of strain rate on deformation response of metastable high entropy alloys upon friction stir processing [J]. Metallurgical and Materials Transactions A, 2020, 51: 5043−5048.
[49] HE Zhu-feng, JIA Nan, WANG H W, LIU Y, LI Dong-yue, SHEN Yong-feng. The effect of strain rate on mechanical properties and microstructure of a metastable FeMnCoCr high entropy alloy [J]. Materials Science and Engineering: A, 2020, 776: 138982.

搅拌摩擦加工制备细晶 $Fe_{40}Mn_{20}Co_{20}Cr_{15}Si_5$ 高熵合金的显微组织演变和拉伸变形行为

林 佳[1]，方 园[2]，王 文[1]，韩 鹏[1]，张 婷[1]，刘 强[1]，向亚婷[1]，强凤鸣[1]，乔 柯[1]，王快社[1]

1. 西安建筑科技大学 冶金工程学院 功能材料加工国家与地方联合工程研究中心，西安 710055；
2. 新疆湘润新材料科技有限公司，哈密 839000

摘 要：采用搅拌摩擦加工(FSP)技术成功制备了具有优异强度和塑性的细晶亚稳双相 $Fe_{40}Mn_{20}Co_{20}Cr_{15}Si_5$ 高熵合金(CS-HEA)。对细晶 CS-HEA 的显微组织和力学性能进行了表征。结果表明，FSP 后，铸态缩孔和元素偏析缺陷被消除，平均晶粒尺寸由 121.1 μm 细化至 5.4 μm，面心立方相分数从 23%增加到 82%。拉伸变形过程中，位错滑移主要发生在 5%~17%应变阶段，相变诱发塑性(TRIP)发生在 17%~26%应变阶段，孪生诱发塑性(TWIP)发生在 26%~ 37%应变阶段。细晶 CS-HEA 的屈服强度、极限抗拉强度和伸长率分别为 503 MPa、1120 MPa 和 37%。该合金强塑性协同效应归因于 TRIP、TWIP、位错强化和细晶强化。

关键词：搅拌摩擦加工；亚稳态高熵合金；细晶显微组织；变形行为；相变诱发塑性

(Edited by Xiang-qun LI)